Solid Freeform Fabrication 2017: Proceedings of the 28th Annual International Solid Freeform Fabrication Symposium – An Additive Manufacturing Conference
Reviewed Paper

Numerical Modeling of High Resolution Electrohydrodynamic Jet Printing Using OpenFOAM

Maxwell Wu, Patrick M. Sammons, Kira Barton
University of Michigan
Department of Mechanical Engineering

Abstract

Electrohydrodynamic jet (e-jet) printing is a micro-/nano-scale additive manufacturing (AM) method that has emerged in recent years as a process to rival similar technologies such as inkjet printing. By utilizing electrostatic forces to induce fluid flow, e-jet has shown the ability to fabricate high resolution features with a wide variety of materials. Because it is a relatively new AM process, the printing behavior of many different types of inks are not completely understood, as existing knowledge of the process relies almost entirely on empirical methods that can be time intensive and difficult to implement for materials that are hazardous or not readily available. This paper discusses procedures for modeling both the electric and fluid dynamics of the e-jet printing process within OpenFOAM, an open-source computational fluid dynamics (CFD) solver. Further discussion has been provided to show simulations of the process at typical high resolution e-jet printing scales and to present existing limitations of the model.

Keywords: Electrohydrodynamic jet printing, CFD, modeling

Introduction

The ability to manufacture devices at the nano- and micro-scale has grown in demand in today's society as nano and micro systems become more widely used in fields such as the medical device [1] and electronics industries [2]. To develop methods for satisfying the resolution and material demands of these systems, a wealth of investigation is currently being performed into a number of different additive manufacturing (AM) methods. One such micro-scale AM method, electrohydrodynamic jet (e-jet) printing, has shown immense promise in meeting the manufacturing requirements of many of these systems. A typical high resolution e-jet printing system consists of a conductive nozzle (orifice diameters between 0.1 and 30 μm), filled with a fluid or "ink" that contains mobile electric charges, positioned at a standoff height (typically between 30 and 200 μm) above an electrically grounded substrate. When a voltage is applied to the nozzle, an electric field is generated between the substrate and the nozzle. The electric field induces charge migration that ultimately leads to ejection of material. By way of the electrohydrodynamically driven fluid ejection, high resolution e-jet printing is able to achieve features smaller than 10μm. These governing physics are in contrast to similar scale AM systems that rely on pressure-driven flow and are limited to features size of approximately 10 to 20 μm. A schematic of the e-jet printing process is depicted in Figure 1.

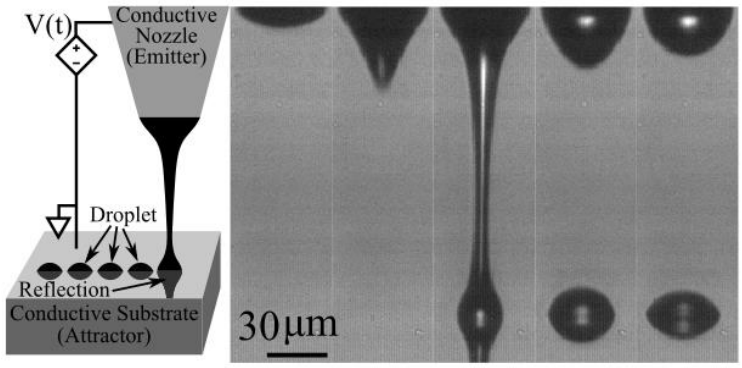

Figure 1: An e-jet printing configuration consists of a charged nozzle at an offset from a conductive, movable substrate

E-jet printing falls into a larger category of processes that are governed by electrohydrodynamics (EHD). While there exist solvers oriented towards modeling systems that are governed by EHD physics, e.g., [3,4], there are several factors that limit the applicability of these methodologies for high resolution e-jet printing; the e-jet printing process that is defined by near field interactions, resulting in sub 10 micron printing resolution. First, many of the existing solvers that have been developed to describe EHD behavior have only been used towards systems at scales larger than those typical of high resolution e-jet printing [4]. It is expected that for reduced length scales, various forces (i.e. surface tension) will have increased influence on system dynamics [5] and therefore the applicability of such solvers at high resolution e-jet printing length scales is unknown. Other solvers have shown the ability to demonstrate EHD behavior at high resolution e-jet printing scales, but have only been used to describe systems with no mass transfer to the environment, such as the solver developed for [3], which simulated electrowetting of pixels at the micron scale. Solvers such as these have shown the ability to accurately model EHD physics, but require validation for simulating systems that exchange mass with their surroundings at high resolution e-jet printing scales.

Many existing solvers that attempt to simulate EHD dynamics have been developed for use within proprietary software such as ANSYS CFX [4], and therefore have limited availability. As commercial software, the code used to run the generic solvers within the program is inaccessible to the user, which limits knowledge of the exact solution methods being employed by the solvers. As an alternative, the model presented here was developed using OpenFOAM, an open-source software that offers greater flexibility to the user, while providing technical support via a wide online user base. Due to its open-source nature, OpenFOAM is a free software package, making it a particularly attractive solution for CFD modeling to reduce experimentation costs. Additionally, user-developed modules are frequently shared publicly, allowing for OpenFOAM to be used for a wide variety of specialized applications. The OpenFOAM solver developed in [3] has been used in this paper to model e-jet printing dynamics at typical high resolution e-jet printing scales.

The remainder of the paper is structured as follows. First, a presentation and discussion of the governing equations within e-jet printing are provided. Then, spatial and temporal mesh

convergence studies are presented for each subsystem within EHD (electrostatics, fluid dynamics, and coupled dynamics). The results of the convergence studies are used in the development of a model of the high resolution e-jet printing system. The final section details conclusions and future work.

Governing Physics and Equations

E-jet printing is reliant upon foundational physics that govern system behavior. Upon applying a voltage to the nozzle, the generated electric field acts upon mobile charges within the ink, causing them to migrate towards or away from the nozzle tip depending on their charge and the applied voltage. This migration creates a local net charge at the nozzle tip as a high concentration of similarly charged particles is formed. However, Coulombic forces generate a repulsive force between these charged particles. As a result, the particles attempt to distance themselves as far away from one another as possible, resulting in a deformation of the ink at the nozzle tip. These electrostatic repulsion forces, in combination with the electric field force, surface tension, and viscous forces results in the formation of a liquid meniscus. Depending on the electric field strength, the balance of these forces can result in a critical meniscus deformation state known as the Taylor cone [6], which is observed as the meniscus is shaped into a conical form that protrudes from the nozzle. As electric field strength is increased, electrostatic forces overcome surface tension and material is ejected from the meniscus towards the substrate.

The governing equations of the leaky-dielectric model are the foundation of the solver that describe fluid deformations resulting from the electrical properties of a system. Equations 1-7 have been adapted from [7] and are presented here to aid the reader. The fluid velocity field, u (m/s), is determined through the Navier-Stokes equations for momentum and continuity of incompressible flow, respectively,

$$\frac{d\rho u}{dt} + \nabla \cdot \rho u u = -\nabla p + \nabla \cdot \left[\mu \left(\nabla u + \nabla u^T \right) \right] + F_\gamma + F_E \tag{1}$$

$$\nabla \cdot u = 0 \tag{2}$$

where ρ (kg/m^3) is fluid density, p (Pa) is fluid pressure, μ (Pa-s) is dynamic viscosity, F_γ (N/m^3) is surface tension force, and F_E (N/m^3) is electrostatic force. Gravitational forces have been determined negligible at the high resolution e-jet printing scale [8] and are not considered.

The electrical conditions of the fluid field are also calculated within the solver. Electric potential, U_E (V), is calculated by Gauss' Law,

$$\nabla \cdot \left(\varepsilon \nabla U_E \right) = -\rho_E \tag{3}$$

where ρ_E (C/m^3) is volumetric charge density and ε (S/m) is the cell permittivity. The charge transport equation

$$\frac{\partial \rho_E}{\partial t} + \nabla \cdot \left(\rho_E u \right) = \nabla \cdot \left(\varepsilon \nabla U_E \right) \tag{4}$$

is employed to solve for charge density. The electric field, E (V/m), is governed by

$$E = -\nabla U_E . \tag{5}$$

The Maxwell Stress Tensor, $\mathbf{T}$ (N/m^2), is then found through

$$\mathbf{T} = \varepsilon \left(EE - \frac{1}{2} |E|^2 \mathbf{I} \right) \tag{6}$$

where $\mathbf{I}$ is the identity matrix. From this, the electrostatic force is determined by

$$F_E = \nabla \cdot \mathbf{T} . \tag{7}$$

Because the e-jet printing process is inherently multiphase, i.e., a fluid system requiring a solution for fluids with different states or material properties, it is necessary to account for changes in material properties throughout the fluid domain. Here, the volume of fluid (VOF) method is used to track behavior at the interface between different fluid phases. The volume fraction of fluid in a cell is calculated as

$$\frac{\partial \alpha}{\partial t} + \nabla \cdot \left(\alpha u \right) - \nabla \cdot \left(\alpha \left(1 - \alpha \right) u_C \right) = 0$$

where α (m^3/m^3) is the primary phase volume fraction and u_C (m/s) is the relative velocity at the interface. The relative interface velocity is determined by

$$u_C = n_f \min \left[C_\gamma \frac{|\phi_m|}{|S_f|}, \max \left(\frac{|\phi_m|}{|S_f|} \right) \right]$$

where n_f is the vector normal to the cell, C_γ is a user defined coefficient (equal to unity in this case), ϕ_m (m^3/s) is the mass flux through the cell, and S_f (m^2) is the cell surface area.

The material properties in each cell (viscosity, density, electrical permittivity, and conductivity) are determined by the primary phase volume fraction and the properties of the independent phases as,

$$\beta = \beta_1 \alpha + \beta_2 \left(1 - \alpha \right) \tag{8}$$

where β represents either the cell density, electrical permittivity, or kinematic viscosity ν (m^2/s), and β_1 and β_2 are the material properties of the primary and secondary phase, respectively.

Tomar [9] observed that for the VOF method, an interface conductivity derived from the harmonic average of the electrical conductivity of the individual phases provides more accurate numerical results. Thus, interface electrical conductivity, σ (S/m), is also calculated according to Eq. 8 where $\beta = 1/\sigma$, $\beta_1 = 1/\sigma_1$ (m/S) is the resistivity of the primary phase and $\beta_2 = 1/\sigma_2$ (m/S) is the resistivity of the secondary phase.

Surface tension forces are calculated according to

$$F_\gamma = \gamma\kappa\left(\nabla\alpha\right)$$

$$\kappa = -\nabla\cdot n = \nabla\cdot\left(\frac{\nabla\alpha}{\left|\nabla\alpha\right|}\right)$$

where γ (N/m) is the surface tension and κ (m^{-1}) is the interface curvature. With all relevant terms of the Navier-Stokes equations accounted for, the fluid flow as a result of the electrostatic behavior of the system can be calculated.

Test Cases

To determine the validity of the solver at typical e-jet printing length scales, several test cases were generated and compared to corresponding analytical solutions. Test cases were designed to test components of the solver independently (i.e. the mechanical equations and electrical equations). Subsequent simulations were conducted to test the solver's ability to solve the coupled electric and mechanical equations in an EHD driven fluid flow.

A. Validation of the Fluid Flow Solver

A test case was created to evaluate the solver's ability to predict mechanically driven fluid flow at a high resolution e-jet printing scale in the absence of electric influences. For this, a laminar, Newtonian, planar Poiseuille flow was modeled, wherein a single incompressible fluid between two long parallel plates is subjected to a constant pressure gradient across the channel length. For pressure driven flow, application of the Navier-Stokes equation with no-slip conditions placed on the plate boundaries leads to a steady state *y*-direction fluid velocity [10],

$$u_y\left(x\right) = \frac{G}{2\mu}\left(h^2 - x^2\right)$$

where u_y (m/s) is the y direction velocity profile along the length of the channel, G is the pressure gradient in the *y*-direction (Pa/m), and the plates are positioned at $x = \pm h$ (m).

In the simulated model, the plates are 120 µm long and separated a distance of 30 µm (i.e. h = 15µm) with arbitrary pressure gradient G = -1/120 Pa/m applied along the channel. The fluid has a dynamic viscosity of μ = 1.0 Pa-s. The ANSYS meshing utility was used to generate a 2-dimensional quadrilateral surface mesh of the domain before conversion to an OpenFOAM format. The mesh and corresponding boundaries are shown in Figure 2. The relevant boundary conditions are provided in Table 1.

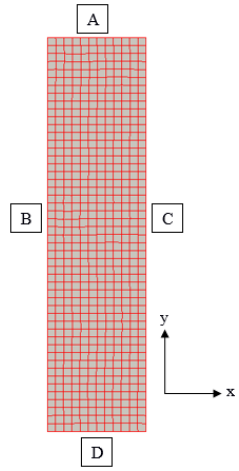

Figure 2: Mesh for 2-D planar Pouiseuille channel flow

Table 1: Boundary conditions for 2-D planar Poiseuille flow

	Boundary Condition				
Boundary	α	p **(Pa)**	u **(m/s)**	ρ_E **(C/m^3)**	U_E **(V)**
A (Wall)	$\nabla\alpha = 0$	$p = 1$	$\nabla u = (0,0,0)$	$\nabla\rho_E = 0$	$U_E = 0$
B (Wall)	$\nabla\alpha = 0$	$\nabla p = 0$	$u = (0,0,0)$	$\nabla\rho_E = 0$	$U_E = 0$
C (Wall)	$\nabla\alpha = 0$	$\nabla p = 0$	$u = (0,0,0)$	$\nabla\rho_E = 0$	$U_E = 0$
D (Wall)	$\nabla\alpha = 0$	$p = 0$	$\nabla u = (0,0,0)$	$\nabla\rho_E = 0$	$U_E = 0$

A mesh refinement study was subsequently performed to monitor solution accuracy and convergence as a function of mesh quality. For this, simulations were conducted using meshes of four different cell lengths and results were compared to the analytical steady state solution after allowing flow to fully develop over 200 seconds of simulation time. Similarly, to determine the effect of time-step size on solution accuracy, a temporal study was conducted wherein simulations were run using five different time-step sizes for each mesh type. Four of the time-step sizes were held at fixed values (0.01s, 0.1s, 1s, and 10s), while a fifth trial utilizes an adaptive time-step, Δt (s) that is determined using a maximum, dimensionless Courant number, $C_{max} = 0.1$, as shown in

$$\Delta t = \frac{C_{\max}}{\frac{u_x}{\Delta x} + \frac{u_y}{\Delta y}} = \frac{0.1}{\frac{u_x}{\Delta x} + \frac{u_y}{\Delta y}}$$

where u_x (m/s) is the x-direction fluid velocity and Δx (m) and Δy (m) are the x- and y- direction cell lengths. This value satisfies the Courant–Friedrichs–Lewy condition (C_{max}<1) for convergence [11], which prevents fluid from passing from one mesh grid point to the next over a single time-step. Simulation results are shown in Figure 3 for a mesh with cell length 3x10^{-7}m. Due to solution convergence, simulation variation for small time steps (0.01s, 0.1s, and the adaptive time step) is reduced. As a result, plot markers for these trials may appear to overlap.

The numerical error with respect to mesh quality and time-step size is shown in Figure 4. It can be seen that smaller time-step sizes lead to greater solution accuracy. Further, when the Courant number is restricted to a small value to prevent solution instability, it can be seen that finer meshes reduce simulation error. Trials utilizing this adaptive time step dictated by a maximum Courant number are depicted as shaded circles in Figure 4.

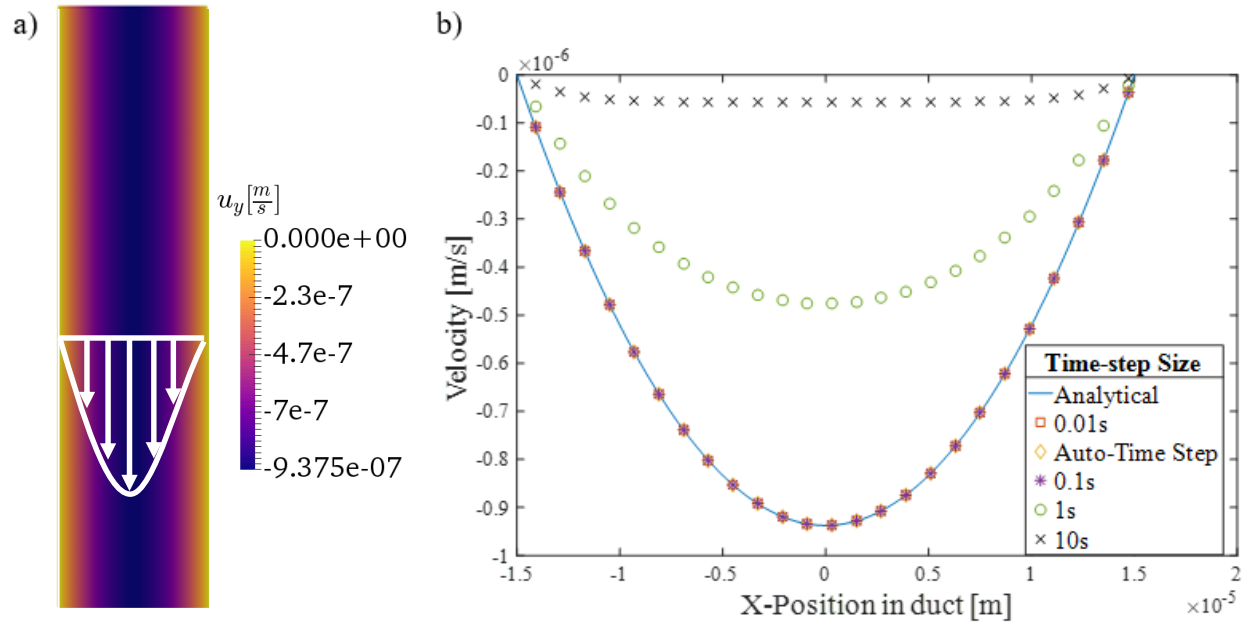

Figure 3: Simulation Results. (a) Screenshot of fully developed y-direction velocity within the channel. (b) Fully developed velocity profile for various time steps for a mesh cell length of $3x10^{-7}$m.

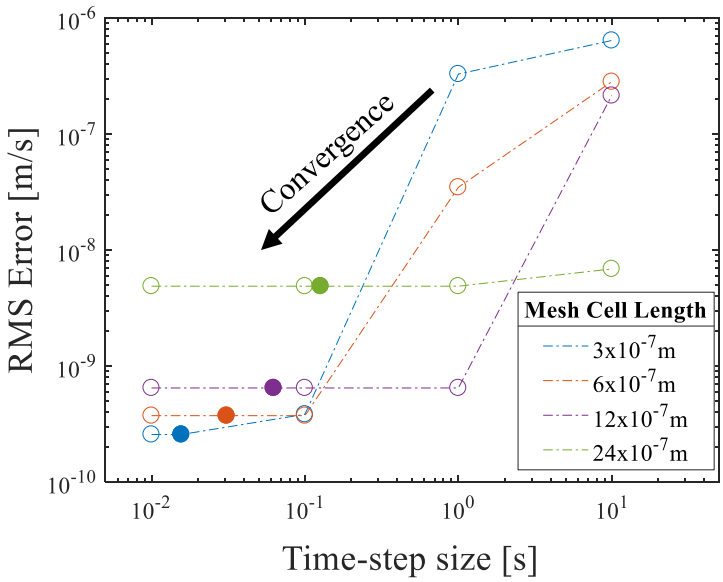

Figure 4: Numerical error with respect to time-step size for various mesh qualities. Simulations restricted by a maximum Courant number are marked with shaded circles

B. Validation of the Electric Solver

A second test case was conducted to evaluate the solver's ability to predict the electric behavior of the system at high resolution e-jet printing length scales through the solution of Gauss' Law and the charge transport equation. A model of a charged, electrically-conductive cylinder in a dielectric, static medium was created, from which the resulting electric field was compared to an analytical solution derived from application of Gauss' Law on a charged conducting rod [12].

The system consists of a 10µm diameter rod with conductivity σ_{rod} = 1 S/m and permittivity ε_{rod} = 1 F/m in the center of a 60µm x 60µm domain with ambient conductivity of σ_{amb} = 1x10^{-20} S/m and permittivity ε_{amb} = 2 F/m. The rod has an initial concentric uniform charge of diameter 8µm with a charge density of 0.5 C/m^3

For conductive materials, internal charges will repel one another and migrate to the surface of the object. This net charge generates an electric field that propagates throughout the dielectric medium. For a cylindrical rod of radius R (m), the generated electric field is,

$$E = \begin{cases} \dfrac{\lambda}{2\pi\varepsilon_{amb} r} & r \geq R \\ 0 & o.w. \end{cases}$$

where E (V/m) is the electric field strength, λ (C/m) is the charge per unit length, and r (m) is the radial distance from the center of the cylinder.

A 2-dimensional quadrilateral cell mesh was generated using the ANSYS meshing utility. Mesh, corresponding boundaries, and the initial simulation domain are shown in Figure 5. The relevant boundary conditions are provided in Table 2.

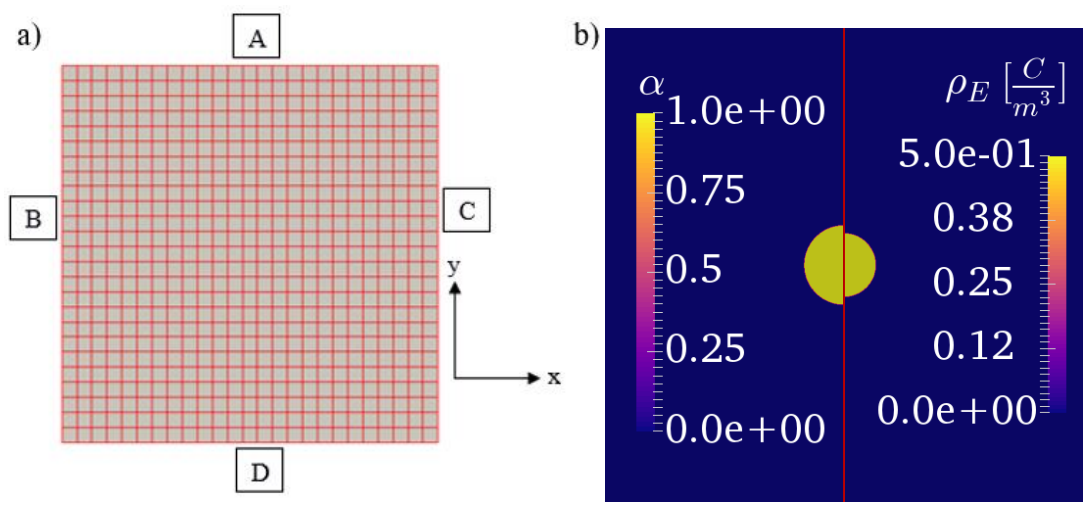

Figure 5: (a) Mesh for 2-D planar charged rod simulations **(b)** Screenshot of the cylinder's initial phase volume fraction across the domain (left) Screenshot of the initial charge density within the domain (right)

Table 2: Boundary conditions for 2-D planar-charged rod in dielectric medium

	Boundary Condition				
Boundary	α	p (Pa)	u (m/s)	ρ_E (C/m^3)	U_E (V)
A (Wall)	$\nabla\alpha = 0$	$p = 0$	$u = (0,0,0)$	$\rho_E = 0$	$U_E = 0$
B (Wall)	$\nabla\alpha = 0$	bouyantPressure	$u = (0,0,0)$	$\rho_E = 0$	$U_E = 0$
C (Wall)	$\nabla\alpha = 0$	bouyantPressure	$u = (0,0,0)$	$\rho_E = 0$	$U_E = 0$
D (Wall)	$\nabla\alpha = 0$	bouyantPressure	$u = (0,0,0)$	$\rho_E = 0$	$U_E = 0$

A mesh study of the model was performed to determine the effect of mesh quality on solution convergence by conducting simulations with four meshes of varying resolution. After 200s of simulation time, the numerical solutions were compared to the analytical steady state solution. Since the magnitude of fluid velocity is small for this case, the time step was based on the electric relaxation time $t_e=\varepsilon/\sigma$ (s). For this simulation, the time step was defined as

$$\Delta t = 0.9\left(\min\left[\frac{\varepsilon_{rod}}{\sigma_{rod}}, \frac{\varepsilon_{amb}}{\sigma_{amb}}\right]\right) = 0.9\,.$$

Simulation results are shown in Figure 6. It can be seen visually that, as predicted, the charges have migrated to the edge of the conducting rod. The trial data shows that there is some error within the simulation, especially at the transition between the inside and outside of the cylinder where there is a discontinuity in the analytical solution. There is also error close to the edge of the simulation domain that may be due to the simulation geometry that uses a rectangular domain. This is in contrast to a radially symmetric analytical solution. It has been observed that this error converges with improved mesh quality. This effect is illustrated in Figure 7.

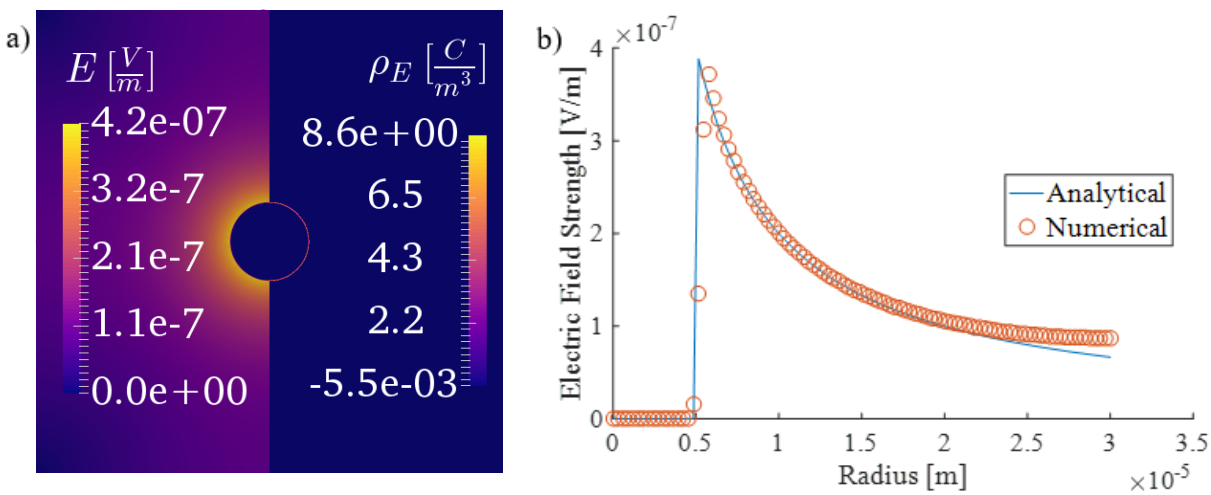

Figure 6: (a) The electric field of the domain after 200s of simulation time (left) Charge density after 200s of simulation time (right) **(b)** Analytical solution for steady state electric field strength versus numerical results obtained using a mesh cell length of 3x10^{-7}m

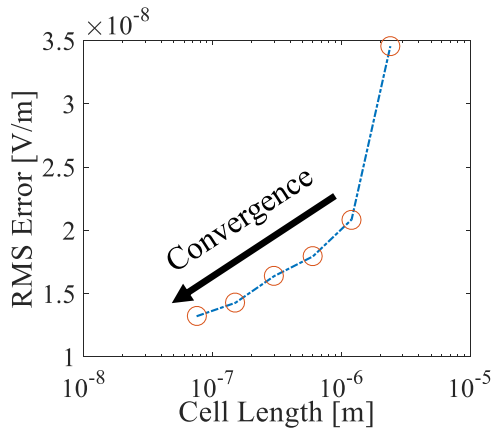

Figure 7: The error of the numerical solver as a function of mesh quality

C. Validation of the Coupled Solver

To validate the ability of the solver to properly determine the coupled fluidic and electrical behavior of a multiphase system simultaneously through the calculation of the Maxwell stress tensor, a model of an electrohydrodynamically driven fluid was created and compared to an analytical solution.

The system consists of a spherical droplet of initial radius R = 10µm with dynamic viscosity μ_{drop} = 1x10^6 Pa-s, conductivity σ_{drop} = 2.5x10^{-4} S/m, and permittivity ε_{drop} = 2x10^{-3} F/m. The droplet is suspended in the center of an axisymmetric domain with a radius of 40µm and height of 80µm, along with dynamic viscosity μ_{amb} = 1x10^6 Pa-s, conductivity σ_{amb} = 1x10^{-4} S/m, and permittivity ε_{amb} = 1x10^{-3} F/m. The interfacial surface tension between the droplet and ambient environment is γ = 1x10^{-4} kg/s^2. A voltage is applied to the bottom wall of the domain while to top wall is electrically grounded. Using this geometry, verification of the solver at high resolution e-jet printing length scales can be achieved.

The quadrilateral-cell mesh was generated with the ANSYS meshing utility and converted to the OpenFOAM format as a 5° axisymmetric wedge. The relevant boundary conditions are provided in Table 3. The mesh and corresponding boundaries, as well as the initial simulation domain are shown in Figure 8.

Table 3: Boundary conditions for axisymmetric suspended droplet deformations

	Boundary Condition				
Boundary	α	p **(Pa)**	u **(m/s)**	ρ_E **(C/m^3)**	U_E **(V)**
A (Wall)	$\nabla\alpha = 0$	$p = 0$	u = (0,0,0)	$\nabla\rho_E = 0$	$U_E = 0$
B (Axis)	Empty	Empty	Empty	Empty	Empty
C (Wall)	$\nabla\alpha = 0$	bouyantPressure	$\nabla u = (0,0,0)$	$\nabla\rho_E = 0$	$\nabla U_E = 0$
D (Wall)	$\nabla\alpha = 0$	bouyantPressure	u = (0,0,0)	$\nabla\rho_E = 0$	U_E = constant

Upon application of an electric field over the domain, the droplet deforms as localized charges generate electrostatic forces. The extent of the deformation is largely dependent upon the non-dimensional electric capillary number, Ca_E, given by

$$Ca_E = \frac{E_\infty^2 R \varepsilon_{amb}}{\gamma}$$

which provides a ratio of the Maxwell stresses to the surface tension forces at the droplet interface where E_∞ (V/m) is the applied electric field.

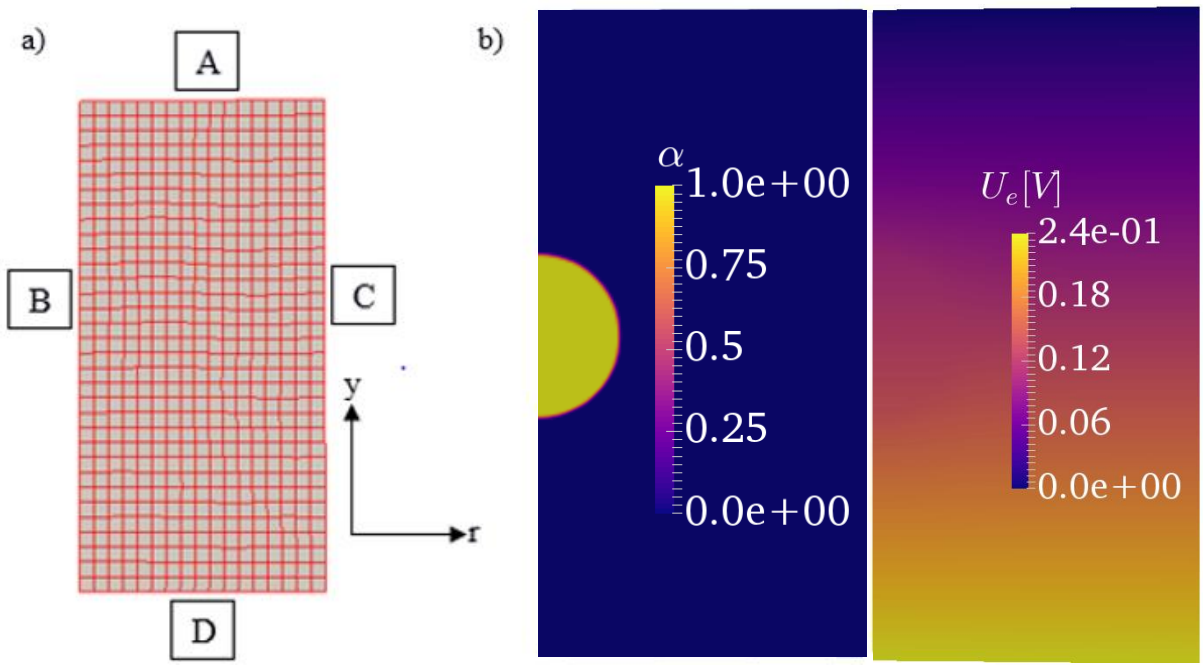

Figure 8: (a) Axisymmetric mesh for suspended droplet deformation simulation **(b)** Screenshot of the initial droplet phase volume fraction (left). Screenshot of the initial electric potential across the domain (right)

G.I. Taylor [13] observed that for small deformations, the droplet's steady state geometry conforms to the scaling law described by,

$$D = \frac{9}{16} \frac{Ca_E}{\left(2 + \frac{\sigma_{drop}}{\sigma_{amb}}\right)^2} \left[1 + \frac{\sigma_{drop}^2}{\sigma_{amb}^2} - 2\frac{\varepsilon_{drop}}{\varepsilon_{amb}} + \frac{3}{5}\left(\frac{\sigma_{drop}}{\sigma_{amb}} - \frac{\varepsilon_{drop}}{\varepsilon_{amb}}\right) \frac{2 + 3\frac{\mu_{drop}}{\mu_{amb}}}{1 + \frac{\mu_{drop}}{\mu_{amb}}} \right]$$
$$= \frac{d_{maj} - d_{min}}{d_{maj} + d_{min}}$$

where D (m/m) is the droplet aspect ratio, and d_{maj} (m) and d_{min} (m) are the length of the droplet's major and minor axes respectively.

Figure 9 depicts results of the simulated droplet geometry after 1,000s had elapsed to allow for steady state to be reached. It is observed that deviation from the analytical solution grows as the electric capillary number is increased, which is expected as the Taylor model is only presumed valid for small droplet deformations.

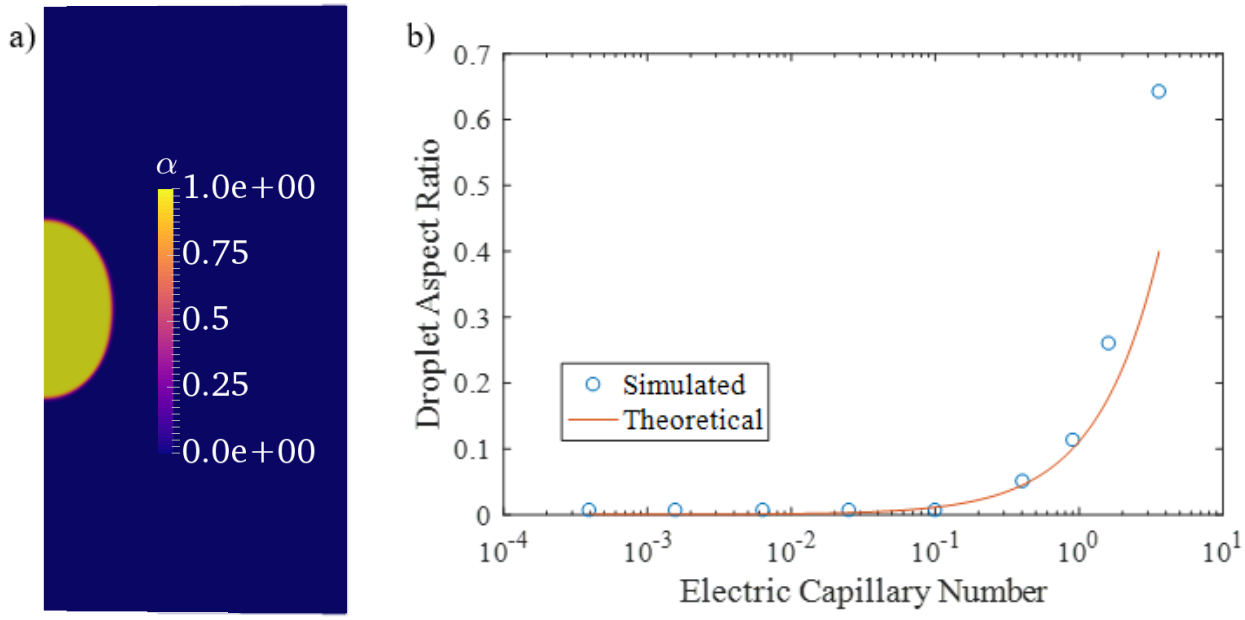

Figure 9: (a) Droplet volume fraction across the domain after application of 0.24V between the top and bottom walls **(b)** The droplet aspect ratio in response to varying electric field strengths

High Resolution E-Jet Printing Case Study

A 2-D axisymmetric model of the e-jet printing system was created in OpenFOAM to demonstrate printing behavior and trends found on a physical printing system. For this, the material properties of hexadecane, a hydrocarbon, was used for the printing ink, with room temperature air properties used for the ambient fluid. Material properties are shown in Table 4 [14-19].

Table 4: Fluid properties used for simulation of Hexadecane printing

Phase	ρ **(kg/m^3)**	ν **(m^2/s)**	ε **(F/m)**	σ **(S/m)**	γ **(N/m)**
1 (Hexadecane)	773	$4.0\text{x}10^{-6}$	$1.815\text{x}10^{-11}$	$1.0\text{x}10^{-13}$	$2.75 \text{ x } 10^{-3}$
2 (Air)	1.2	$1.51\text{x } 10^{-5}$	$8.854\text{x } 10^{-12}$	$5.0\text{x}10^{-15}$	

The modeled system was composed of a 30 µm diameter nozzle positioned at a 70 µm standoff height from an electrically grounded substrate. The nozzle was initially filled with hexadecane with no protruding meniscus. The quadrilateral-cell mesh is 30µm x 80 µm and was generated using the ANSYS meshing utility before conversion into a 5° axisymmetric wedge for use in OpenFOAM. The mesh and corresponding boundaries, as well as the initial simulation domain are shown in Figure 10. Boundary conditions are provided in Table 5.

Chen, Saville, and Aksay [20] has shown that an increasing input voltage results in larger volumetric flow rates. To test the solver's ability to replicate this phenomenon, a parametric study

was performed on the effect of nozzle input voltage on volumetric flow rate. The nozzle was charged for 3.3×10^{-5}s at voltages of 1500V, 1750V, 2000V, 2250V, 2500V, and 2750V before a measurement of the total volume of hexadecane within the domain was determined. Simulation results are shown in Figure 11.

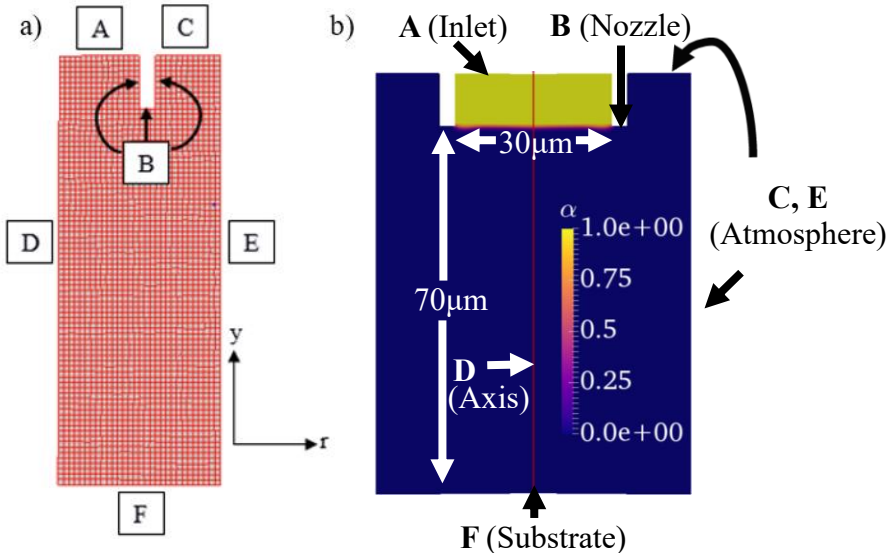

Figure 10: (a) Mesh for e-jet printing simulation **(b)** Screenshot of initial hexadecane volume fraction. The image of the domain has been mirrored across the central axis (D) for clarity.

Table 5: Boundary conditions for e-jet printing simulations

	Boundary Condition				
Boundary	α	p **(Pa)**	u **(m/s)**	ρ_E **(C/m^3)**	U_E **(V)**
A (Inlet)	$\alpha = 1$	$p = 400$	pressureInlet OutletVelocity	$\nabla \rho_E = 0$	$\nabla U_E = 0$
B (Nozzle Wall)	$\nabla \alpha = 0$	fixedFlux Pressure	$u = (0,0,0)$	$\nabla \rho_E = 0$	U_E = const.
C, E (Atmosphere)	$\begin{cases} \nabla \alpha = 0 & \text{outflow} \\ \alpha = 0 & \text{inflow} \end{cases}$	$p = 0$	pressureInlet OutletVelocity	$\nabla \rho_E = 0$	$\nabla U_E = 0$
D (Axis)	Empty	Empty	Empty	Empty	Empty
F (Substrate Wall)	$\nabla \alpha = 0$	fixedFlux Pressure	$u = (0,0,0)$	$\nabla \rho_E = 0$	$U_E = 0$

It was observed that for input voltages of 1500V and 1750V fluid was not ejected from the nozzle, even when simulation time was increased. This resulted in a non-growing meniscus forming at the nozzle tip as electrostatic forces were not able to overcome surface tension. For larger voltages, it can be seen that the total volume of hexadecane within the simulation domain, and therefore volumetric flow rate, increase with input voltage as the fluid continuously approaches the substrate. These results agree with predictions based on [20].

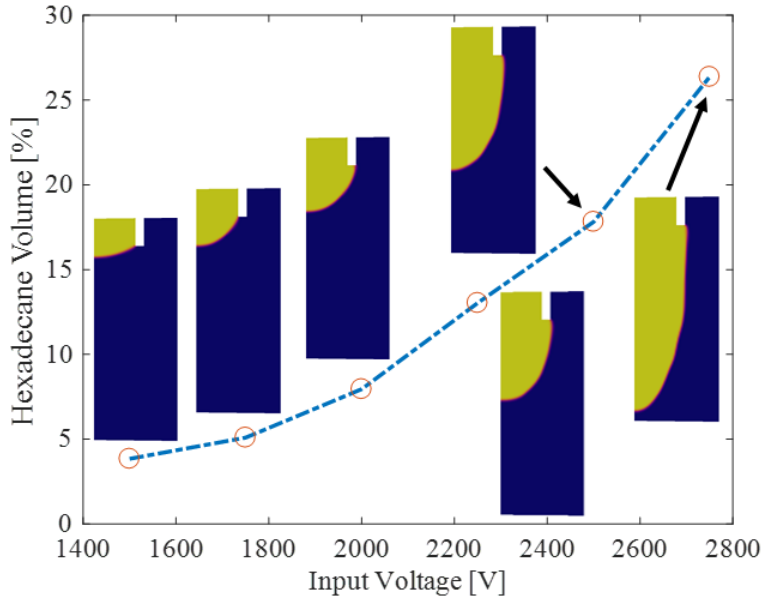

Figure 11: The effect of varying input voltage on the hexadecane volume as a percentage of the total domain volume after 3.3×10^{-5}s

Conclusions

This document presented an initial approach towards developing a CFD model of electrohydrodynamics at the high resolution e-jet printing scale. Through the use of an OpenFOAM solver initially developed in [3], such modeling is accomplished in a highly flexible and cost-effective manner to solve the fundamental equations of EHD. The solver implements the volume-of-fluid (VOF) method to determine electrical properties of the system such as the electric potential and charge density, and model the effect of these properties on mechanical behavior of the system through a calculation of the Maxwell stress tensor.

At present, the simulations have shown immense promise in providing a manipulable model of the e-jet printing system and can be easily modified to reflect a wide variety of different materials and voltage inputs. The solver's accuracy at the high resolution e-jet printing scale has been verified through a series of test cases, and further results have demonstrated the ability to reproduce experimental data. However, further studies will be required to determine the solver's robustness with regards to simulating varying printing geometries or varied printing environments. Such work will assist in expediting future research into e-jet printing behavior.

References

[1] Gittard, S.D., Narayan, R.J., "Laser Direct Writing of Micro- and Nano-scale Medical Devices," *Expert Review of Medical Devices*, Volume 7 (2010), pp. 343–356.

[2] Gomez De Arco, L., Zhang, Y., Schlenker, C.W., Ryu, K., Thompson, M.E., Zhou, C., "Continuous, Highly Flexible, and Transparent Graphene Films by Chemical Vapor Deposition for Organic Photovoltaics," *ACS Nano*, Volume 4 (2010), pp. 2865–2873.

[3] Roghair, I., Musterd, M., van den Ende, D., Kleijn, C., Kreutzer, M., Mugele, F., "A Numerical Technique to Simulate Display Pixels Based on Electrowetting," *Microfluidics and Nanofluidics*, Volume 19 (2015), pp. 465–482.
[4] Lastow, O., Balachandran, W., "Numerical Simulation of Electrohydrodynamic (EHD) Atomization," *Journal of Electrostatics*, Volume 64 (2006), pp. 850 – 859.
[5] Ho, C.M., "Micro/Nano Technology Systems for Biomedical Applications: Microfluidics, Optics, and Surface Chemistry," Oxford University Press, Oxford, (2010).
[6] Wilm, M.S., Mann, M., "Electrospray and Taylor-Cone Theory, Dole's Beam of Macromolecules at Last?," *International Journal of Mass Spectrometry and Ion Processes*, Volume 136 (1994), pp. 167 – 180.
[7] Saville, D.A., "Electrohydrodynamics: The Taylor-Melcher Leaky Dielectric Model," *Annual Review of Fluid Mechanics*, Volume 29 (1997), pp. 27–64.
[8] Choi, H.K., Park, J.-U., Park, O.O., Ferreira, P.M., Georgiadis, J.G., Rogers, J.A., "Scaling Laws for Jet Pulsations Associated with High-Resolution Electrohydrodynamic Printing," *Applied Physics Letters*, Volume 92 (2008), 123109:1-3.
[9] Tomar, G., Gerlach, D., Biswas, G., Alleborn, N., Sharma, A., Durst, F., Welch, S.W.J., Delgado, A., "Two-Phase Electrohydrodynamic Simulations Using a Volume-of-Fluid Approach," *Journal of Computational Physics*, Volume 227 (2007), pp. 1267 - 1285.
[10] Langlois, W.E., Deville, M.O. "Slow viscous flow," Springer International Publishing, Berlin, (2014).
[11] Courant, R., Friedrichs, K.O., Lewy, H., "On the Partial Difference Equations of Mathematical Physics," *IBM Journal of Research and Development*, Volume 11, pp. 215–235, (1967).
[12] Ohanian, H.C., Markert, J.T., "Physics for Engineers and Scientists." 3rd ed., W.W. Norton & Co., New York, (2007).
[13] Taylor, G.I., "Studies in Electrohydrodynamics. I. The Circulation Produced in a Drop by Electrical Field," *Proceedings of the Royal Society of London. Series A, Mathematical and Physical Sciences*, Volume 291 (1966), pp. 159–166.
[14] National Center for Biotechnology Information. PubChem Compound Database; CID=11006, https://pubchem.ncbi.nlm.nih.gov/compound/11006 (accessed June 15, 2017).
[15] Dymond, J. H., Young, K. J., "Transport Properties of Nonelectrolyte Liquid Mixtures—I. Viscosity Coefficients for n-Alkane Mixtures at Saturation Pressure from 283 to 378K," *International Journal of Thermophysics*, Volume 1, (1980), pp. 331–344.
[16] Hahn, G., Svejda, P., Dallos, A., "Volumetric and Dielectric Properties of the Binary Liquid Systems: 1,2-Dichloroethane + n-Alkanes or + 2,2,4-Trimethylpentane," *Fluid Phase Equilibria*, Volume 86, (1993), pp. 293 – 313.
[17] Hayati, I., Bailey, A.I., Tadros, T.F., "Investigations into the Mechanisms of Electrohydrodynamic Spraying of Liquids," *Journal of Colloid and Interface Science*, Volume 117, (1987), pp. 205 –221.
[18] Haynes, W.M., ed., "CRC Handbook of Chemistry and Physics, 97th Edition (Internet Version 2017)," CRC Press/Taylor & Francis, Boca Raton, FL., (2017).
[19] Pawar, S.D., Murugavel, P., Lal, D. M., "Effect of Relative Humidity and Sea Level Pressure on Electrical Conductivity of Air over Indian Ocean," *Journal of Geophysical Research: Atmospheres*, Volume 114, (2009), 10.1029/2007JD009716:1-8
[20] Chen, C.H., Saville, D.A., Aksay, I.A., "Scaling Laws for Pulsed Electrohydrodynamic Drop Formation," *Applied Physics Letters*, Volume 89, (2006), 124103:1-3.